Asymmetric ground states in La$_{0.67}$Sr$_{0.33}$MnO$_3$/BaTiO$_3$ heterostructures induced by flexoelectric bending

Mingqun Qi, Zhen Yang, Shengru Chen, et al.

View Online   Export Citation   CrossMark

ARTICLES YOU MAY BE INTERESTED IN

Asymmetric ground states in La$_{0.67}$Sr$_{0.33}$MnO$_3$/BaTiO$_3$ heterostructures induced by flexoelectric bending

Mingqun Qi,[1,2] Zhen Yang,[2,3] Shengru Chen,[2,3] Shan Lin,[2,3] Qiao Jin,[2,3] Haitao Hong,[2,3] Dongke Rong,[2] Haizhong Guo,[4] (iD) Can Wang,[2,3,5] Ziyu Wang,[6] (iD) Kui-Juan Jin,[2,3,5,a)] Zhenping Wu,[1,a)] (iD) and Er-Jia Guo[2,3,5,a)] (iD)

AFFILIATIONS

[1]State Key Laboratory of Information Photonics and Optical Communications and Laboratory of Optoelectronics Materials and Devices, School of Science, Beijing University of Posts and Telecommunications, Beijing 100876, China
[2]Beijing National Laboratory for Condensed Matter Physics and Institute of Physics, Chinese Academy of Sciences, Beijing 100190, China
[3]University of Chinese Academy of Sciences, Beijing 100049, China
[4]Key Laboratory of Material Physics, Ministry of Education, School of Physics and Microelectronics, Zhengzhou University, Zhengzhou 450001, China
[5]Songshan Lake Materials Laboratory, Dongguan, Guangdong 523808, China
[6]The Institute of Technological Sciences, Wuhan University, Wuhan 430072, People's Republic of China

[a)]Authors to whom correspondence should be addressed: kjjin@iphy.ac.cn; zhenpingwu@bupt.edu.cn; and ejguo@iphy.ac.cn

ABSTRACT

Misfit strain delivered from single-crystal substrates typically modifies the ground states of transition metal oxides, generating increasing interest in designing modern transducers and sensors. Here, we demonstrate that magnetotransport properties of La$_{0.67}$Sr$_{0.33}$MnO$_3$ (LSMO) films were continuously tuned by uniaxial strain produced by a home-designed bending jig. The electrical conductivity and Curie temperature of LSMO films are enhanced by bending stresses. The resistivity of *u*-shape bended LSMO decays three times faster than that of *n*-shape bended LSMO as a response to the same magnitude of strain. The asymmetric magnetic states in uniaxially strained LSMO are attributed to the dual actions of Jahn–Teller distortion and strain gradient mediated flexoelectric fields in an adjacent ferroelectric layer. These findings of multi-field regulation in a single material provide a feasible means for developing flexible electronic and spintronic devices.

Published under an exclusive license by AIP Publishing. https://doi.org/10.1063/5.0092134

Flexible electronics have witnessed impressive progress in wearable sensing, environmental monitoring, energy chemistry, and biomedicine.[1–7] As listed in one of the top ten scientific and technological projects, flexible materials and their related devices inevitably promote a major industrial revolution in the future.[8] By then, our daily life and work will be greatly benefited from these innovation technologies.[9] Typically, electronic devices mainly make use of their single physical properties of existing flexible materials such as high conductivity and high transmission.[10–12] The integration of complex materials with multiple properties is essential for developing smaller, smarter, and low-power consuming devices. To date, the flexible devices based on the complex oxides have not been explored extensively due to the limitation of their rigid and single-crystalline substrates.[13] Typically, these substrates are used for oxide thin film growth due to the compatible crystallographic symmetry and small lattice mismatch. However, these single crystal substrates are extremely fragile and non-foldable. The as-grown thin films are inflexible even though the thickness of substrates was reduced to the sub-micrometer scale. This fact inevitably limits the investigations of wide-range strain effects on their physical properties and prevents their potential applications toward flexible devices.

van der Waals (vdW) heteroepitaxy has been proposed initially to demonstrate the epitaxial growth of two-dimensional (2D) layered materials on other 2D layered materials. This method has been extended to describe the epitaxial growth of functional oxides on 2D materials.[14–16] For instance, Chu's group had successfully fabricated various oxides on the layered fluoropolytic-mica (Mica) substrates.[17–20] One of the key advantages of vdW epitaxy is the weak interaction between films and substrates, leading to a large tolerance in

the lattice mismatch and crystallographic symmetry.[21] Therefore, oxides with different crystallographic structures can be epitaxially grown on mica with relatively high quality.[22–25] These oxide films are no longer clamped by mica substrates, resulting in a nearly strain-free virgin state. Most importantly, the layered character of mica makes it very flexible and easy to be folded under large bending stress, providing a playground for studying strain effects on the physical properties of transition metal oxides. The high thermal and chemical stability also allows mica to be used as appropriate high-temperature substrates for thin-film growth.[21] In this Letter, we fabricated the heterostructures composed of ferromagnetic $La_{0.67}Sr_{0.33}MnO_3$ (LSMO) and ferroelectric $BaTiO_3$ (BTO) layers. The magnetoelectric characteristics of LSMO were investigated by applying uniaxial strain ranging from −2% to 2% using a home-designed bending jig. We find that the conductivity and Curie temperature (T_C) exhibit an asymmetric response under the same magnitude of bending stress. The unique behavior is attributed to both intrinsic structural distortions induced electronic modification and extrinsic ferroelastic effects from an adjacent ferroelectric layer.

The heterostructures composed of BTO and LSMO were grown on (001)-oriented mica and (111)-oriented STO substrates simultaneously using pulsed laser deposition (PLD).[26] The LSMO/BTO and BTO/LSMO/BTO trilayers were fabricated for strain-tuning. The thicknesses of BTO and LSMO thin layers are 15 and 50 nm, respectively. The BTO layer was used as a buffer layer to minimize misfit strain between LSMO and mica.[27] During deposition, the substrate's temperature was kept at 750 °C, and oxygen partial pressure was maintained at 200 mTorr. The laser frequency and energy density were kept as 5 Hz and ∼1.0 J/cm², respectively. The samples were cooled down slowly to room temperature at a rate of −5 °C/min under the oxygen partial pressure of 100 Torr. X-ray diffraction (XRD) measurements were performed using a Bruker D8 Discovery high-resolution diffractometer with Cu Kα1 radiation (Fig. S1, supplementary material). XRD θ–2θ scans reveal that all layers are epitaxially grown without impurity phases. Reciprocal space mapping around mica substrate's 00l reflections was measured using a Panalytical X'Pert MRD four-circle x-ray diffractometer. RSM results demonstrate that LSMO/BTO bilayers are epitaxially grown along the (111) orientation. We calculate the inter-planar spacings for LSMO (111) and BTO (111) layers on (111)-STO substrates are 2.224 Å (∼2.254 Å for LSMO bulk) and 2.281 Å (∼2.314 Å for BTO bulk), respectively. The LSMO film is under the substrate-induced tensile-strain, leading to the out-of-plane lattice constant shrinks by ∼1.3%. In contrast, the BTO and LSMO films grown on mica are almost strain-free, similar to the previous reports. Therefore, the virgin strain state of as-grown LSMO films on mica substrates is close to its bulk form.[28]

The electrical transport and magnetic properties of LSMO films on (111)-STO and mica substrates were measured using a physical properties measurement system (PPMS) and magnetic property measurement system (MPMS), respectively. Figure 1(a) shows the M–T
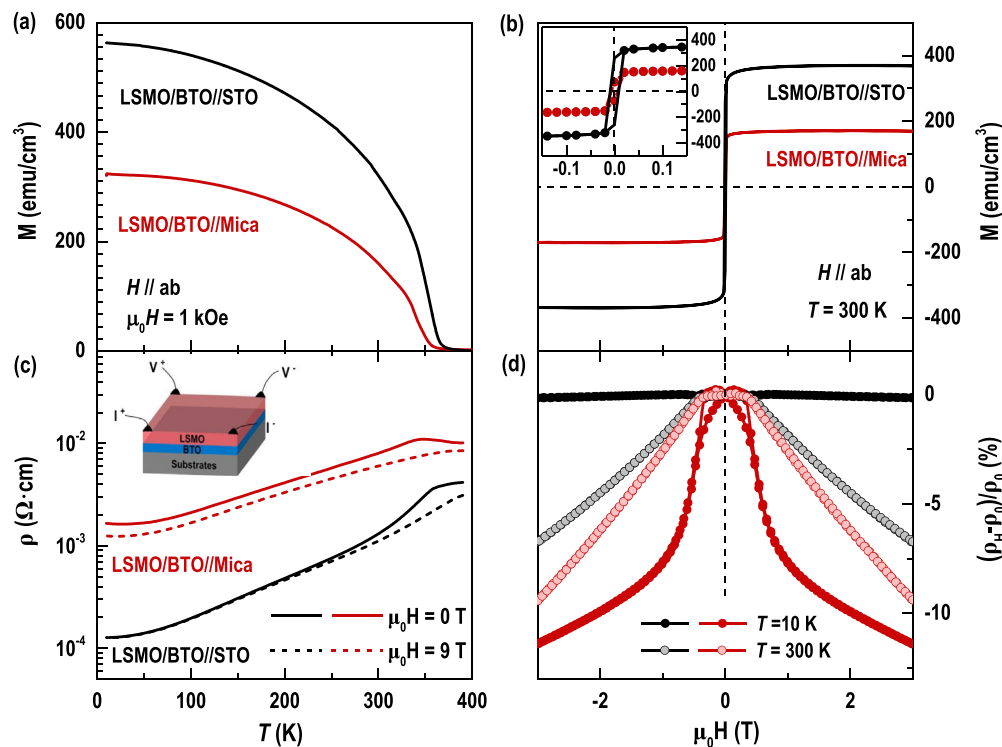

FIG. 1. Transport properties of LSMO/BTO bilayers at virgin states. Temperature dependent (a) in-plane magnetization (M) and (c) resistivities (ρ) of LSMO/BTO bilayers on STO (black lines) and mica (red lines) substrates. M–T curves were recorded at 1 kOe after field-cooling. ρ−T curves were measured at 0 T(solid line) and 9 T (dashed line). Inset shows the geometry of electrical measurements using the van der Pauw method. Field dependent (b) M (300 K) and (d) magnetoresistances [MR = $(\rho_H−\rho_0)/\rho_0$] for LSMO/BTO bilayers on STO and mica substrates at 10 and 300 K.

curves of LSMO/BTO bilayers at an in-plane magnetic field of 1 kOe. The T_C of LSMO films on mica is ~350 K, whereas the T_C of LSMO films on (111)-STO is ~370 K, which is close to the T_C of bulk LSMO.[29] The lower T_C of LSMO films on mica is likely due to different microstructures and strain states in the as-grown films. Room-temperature magnetic hysteresis loops yield that the coercive fields of both LSMO/BTO bilayers are around 100 Oe [the inset of Fig. 1(b)]. The LSMO films grown on (111)-STO show a higher saturation moment than those of LSMO films grown on mica. The resistivities (ρ) and magnetoresistances [MR $= (\rho_H - \rho_0)/\rho_0$] were measured using the van der Pauw method, where ρ_0 and ρ_H are the resistivities under magnetic fields of 0 and 9 T, respectively. The resistivities of LSMO films obtained from two geometries, i.e., one is the current passed along the bending direction and another is the current passed perpendicular to the bending direction, are almost equivalent. Thus, the resistivities of LSMO films were averaged from those values. Figure 1(c) shows the ρ–T curves of both LSMO/BTO bilayers. The LSMO layers exhibit a clear insulator-to-metal transition with decreasing temperature. This is a typical characteristic of the hole-doped manganites.[30–32] The LSMO films on mica exhibit a larger ρ than that of LSMO on (111)-STO substrates. At 10 K, ρ of LSMO on mica is more than one order of magnitude larger than that of LSMO on STO. The field-dependent MR at 10 and 300 K were present in Fig. 1(d). The MR of LSMO films shows negative values under external fields, demonstrating the ferromagnetic characteristic of LSMO. At 10 K, the MR shows symmetric peaks at small fields corresponding to its coercive fields

(H_C). When T increases to 300 K, the MR of LSMO on mica reduces slightly, and the butterfly like hysteresis loop disappears. Instead, the MR keeps nearly unchanged at small fields and starts to decrease linearly when the magnetic fields exceed H_C.

Typically, mica can be mechanically exfoliated down to 10 μm in thickness due to the interlamellar vdW bonding characteristics.[21,33] The ultrathin mica allows them to be bended substantially. We designed a mechanical bending jig to apply uniaxial strain to the samples. The strain states of as-grown films can be *in situ* controlled and maintained by bending forces during the measurements (Fig. S2, supplementary material). The center position of samples was bended in "*u*-shape" or "*n*-shape." A high-resolution camera with a fixed position was used to capture the sample's positions and bending curvatures under different strain states (Fig. S3, supplementary material).[26,34] We quantified the uniaxial strain of LSMO films induced by mechanical forces using bending parameters, e.g., the length of sample's bending part and the deformation displacement at the center positions. The strain states are directly linked to their physical properties. Figures 2(a) and 2(b) show the zero-field ρ–T curves of LSMO films under switchable bending stresses. The maximum bending stresses were achieved up to −2% and 1.8%, respectively. The ρ of LSMO films reduces progressively by increasing uniaxial stress. Figure 2(c) summarizes the change rate of resistivity [$\Delta\rho = (\rho_{strain} - \rho_{virgin})/\rho_{virgin}$] as a function of stress at 150, 300, and 350 K. Compared to the tensile strain cases, the ρ of LSMO films decays rapidly when the uniaxial stress reduces from the virgin state to −1% and slows down when compressive strain beyond −1%.
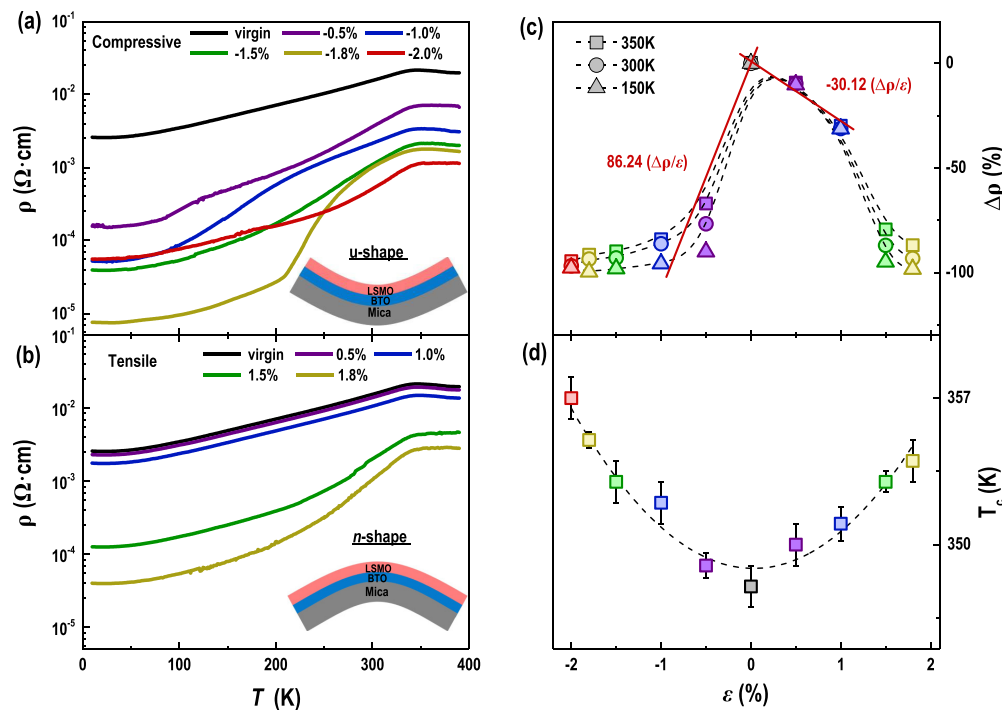

FIG. 2. Tunable ground states of LSMO/BTO bilayers under various uniaxial stresses. Zero-field ρ-T curves of LSMO/BTO bilayers under various (a) compressive and (b) tensile stresses. Insets show the schematic of sample status, i.e., *u*-shape and *n*-shape bendings correspond to compressive and tensile stresses, respectively. (c) The resistivity ratios [$\Delta\rho = (\rho_{strain} - \rho_{virgin})/\rho_{virgin}$] and (d) Curie temperatures (T_C) were plotted as a function of stress. The $\Delta\rho$ at 150, 300, and 350 K exhibit the similar asymmetric stress dependency.

The $\Delta\rho(\varepsilon)$ in a compressive stress regime is almost three times larger than that of a tensile stress regime. T_C enhances at nearly a constant ratio of ~5 K per 1% as the bending stress increases [Fig. 2(d)].

Intriguing magnetotransport properties of LSMO films were further investigated when LSMO films were under different stresses. Figure 3(a) shows the typical butterfly like hysteresis loops of MR at 10 K when the stress switches from the compressive state ($\varepsilon = -2\%$) to the tensile state ($\varepsilon = 1.8\%$). MR measured at different stress states exhibits similar variation trends, i.e., positive MR at small fields and negative MR at high fields. We derive H_C from the symmetric peaks of MR. Figure 3(b) presents the H_C of LSMO films as a function of stress at various temperatures. With increasing temperature and stress, H_C decreases distinctly. Generally, the H_C of LSMO films under compressive stresses is smaller than that of the tensile-stressed LSMO films. In particular, we observe unique double symmetric peaks on MR loops when $\varepsilon = -2\%$.[35–37] We hypothesize that the LSMO films break into two magnetic layers that exhibit different H_C when the uniaxial strain exceeds 2%. Figure 3(c) summarizes the MR as a function of stress at 10 K when $\mu_0H = 0.5$ and 3 T. The stress reduces MR($\mu_0H = 3$ T) by a factor of two, and this effect decreases at small magnetic fields.

The stress dependent asymmetric behaviors in magnetotransport properties of LSMO films demonstrate that additional impact factors control the ground states of LSMO films. The basic unit cell of mica contains two silicate tetrahedral sheets (SiO_4) on both sides of an aluminum octahedron (AlO_6). The layers with strong covalent bonding, however, are weakly stacked together by interlayer cations, resulting in

a vdW gap of ~1 nm. The cleavage of mica along the vdW gap layer produces the fresh, atomically flat surface with randomly distributed cations. These cleaved mica substrates preserve the charge neutral surfaces, which are ideal for vdW oxide epitaxy. Experimentally, we determine that the BTO films grown on mica exhibit an intrinsic upward ferroelectric polarization using a piezoelectric force microscope (Asylum Research MFP3D) (Fig. S4, supplementary material). Mechanically bending forces will generate a strain gradient along the in-plane direction, resulting in a flexoelectric field perpendicular to the surface plane. The magnitude of the flexoelectric field is proportional to the strain gradient, i.e., the bending curvature.[38–40] Apparently, the u-shape and n-shape bending statuses produce opposite flexoelectric fields, which are responsible for the asymmetric ground states of LSMO under compressive and tensile strains. The flexoelectric modulation to transport properties of LSMO is similar to the ferroelectric control of conductivity at the BTO/LSMO interface. In the u-shape bending status, the flexoelectric field in BTO layers points upward; thus, the electrons accumulate at the LSMO/BTO interfaces. Thus, the ρ reduces rapidly and T_C enhances dramatically in the compressively stressed LSMO films compared to those of tensile-stressed LSMO cases (corresponding to the hole accumulation). However, although the flexoelectric field effects play a significant role in the small strain regime, we believe the modulation of ρ should be dominated by uniaxial strain-induced Jahn-Teller distortion instead of the flexoelectric polarization in a large strain regime. Therefore, the reduction of ρ is almost the same under both maximum bending stresses.
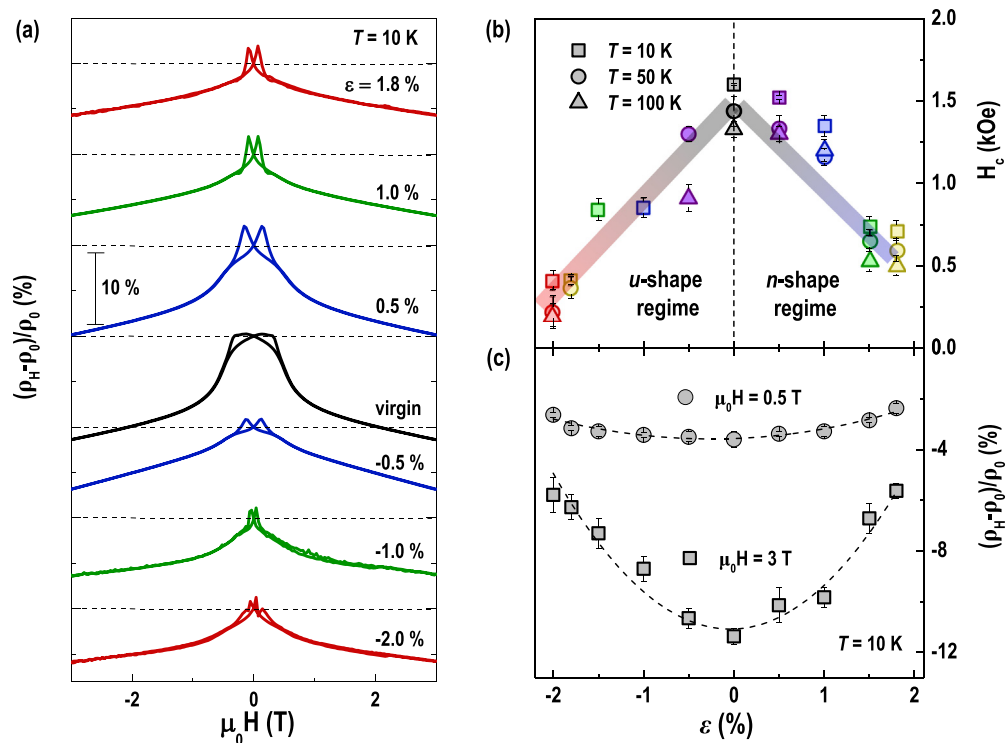

FIG. 3. Magnetotransport properties of a LSMO/BTO bilayer under various stresses. (a) Field dependent MR at 10 K for the uniaxial stress changes from −2% to 1.8%. The MR is up-shifted for clarification. Stress dependent (b) coercive fields (H_C) and (c) MR. H_C was derived from hysteresis loops recorded at 10, 50, 100, and 150 K. MR was recorded at 10 K under magnetic fields of 0.5 and 3 T.
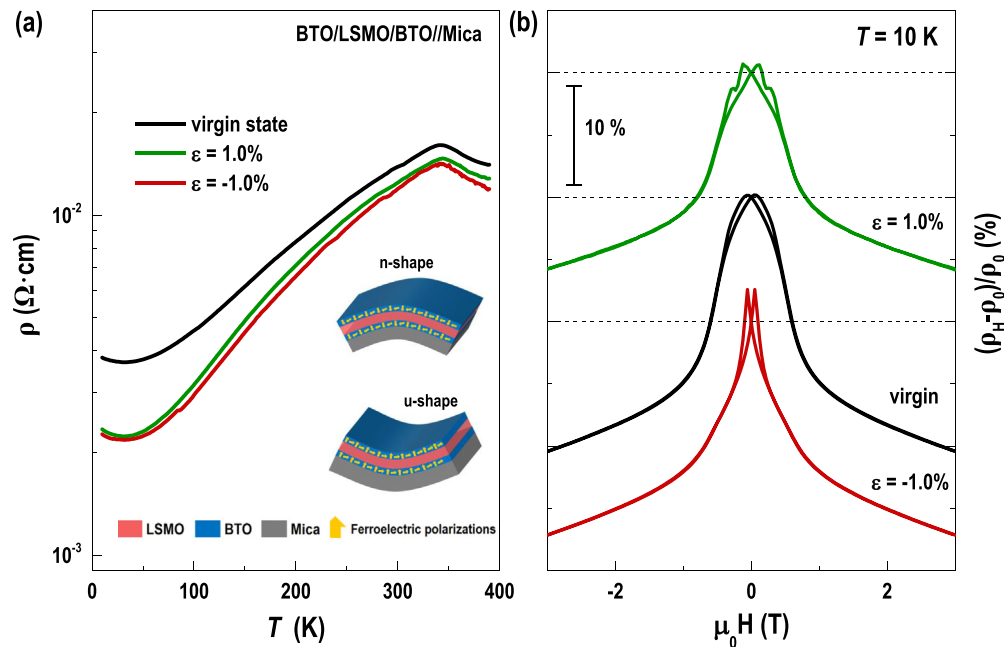
FIG. 4. Magnetotransport measurements on a BTO/LSMO/BTO trilayer under symmetric compression and extension. (a) Temperature dependent ρ of the BTO/LSMO/BTO trilayer under different uniaxial stresses of -1%, 0%, and 1%. Inset shows the schematics of sample geometry under compression (u-shape) and extension (n-shape). The yellow arrows indicate the ferroelectric polarization induced by stress-induced flexoelectric fields. (b) Field dependent MR at 10 K under different stresses of -1%, 0%, and 1%. The MR is up-shifted for clarification.

To eliminate the flexoelectric effects on the transport properties of LSMO films, we sandwiched a LSMO film between two BTO layers with equal thicknesses. The top and bottom BTO layers generate identical flexoelectric polarization within the layers. Therefore, one interface of LSMO layers is hole accumulation, while the other interface is hole depletion, or vice versa, depending on the bending status. The magnitude of interfacial charge doping effects is equal when LSMO films are in both bending statuses. Figure 4(a) shows the ρ–T curves of BTO/LSMO/BTO trilayers at a virgin state, a compressive strain state, and a tensile strain state. The virgin LSMO film presents an insulator-to-metal transition at a temperature of $\sim$347 K, which is identical to that of LSMO/BTO bilayers. The ρ of a BTO/LSMO/BTO trilayer is three times larger than the resistivity of LSMO/BTO bilayers, and meanwhile, it exhibits a low-temperature upturn. These results may attribute to the structural distortion induced weak localization.[41,42] We notice that the ρ of BTO/LSMO/BTO trilayers reduces only 10% and the T_C increases only $\sim$1 K upon the mechanical bendings in sharp contrast to the results of LSMO/BTO bilayers, further highlighting the previously discussed flexoelectric effects at the small stress regime. The genuine uniaxial strain effects on magnetotransport properties of LSMO films were further investigated under different strain states (Fig. S5, supplementary material). Similar to the bilayer's results, H_C reduces with increasing uniaxial stress. Figure 4(b) presents MR as a function of magnetic fields when $\varepsilon = -1\%$, 0%, and 1%. The symmetric peaks at small fields appear in the hysteresis loop when the trilayer is in the virgin and compressive-stress states. However, we notice that the MR curves of tensile-strained LSMO films exhibit four distinct peaks. These results suggest that the LSMO films possibly break into

two magnetic layers under large uniaxial tensile strains. Different parts of LSMO films exhibit independent magnetic switching behaviors. Thus, the MR curves possess multiple peaks, corresponding to different H_C in the hysteresis loops.

In summary, we report the dual actions of uniaxial stress and flexoelectric fields on the transport properties of LSMO films in proximity to ferroelectric materials. The uniaxial stresses were *in situ* continuously controlled in a wide range from -2% to 1.8% using a home-designed bending jig. We find that the stress effect on the electrical conductivity and magnetoresistance is nonlinear. We hypothesize that the asymmetric magnetoelectric responses can be attributed to the flexoelectric fields generated by uniaxial stress, which manifests the carrier density of LSMO films. Our results shed intensive insight on the strong competition between the charge and lattice degrees of freedom in the functional oxides. Additionally, the design of highly stress-sensitive flexible devices paves a potential route toward the neoteric strain sensors.

See the supplementary material for additional information about the structural characterizations, bending jig photograph, calibration of bending stress, piezoresponse force microscopy characterizations, and magnetoresistance measurements.

AUTHOR DECLARATIONS
Conflict of Interest

The authors have no conflicts to disclose.

Author Contributions

Mingqun Qi: Data curation (lead); formal analysis (equal). **Zhen Yang:** Resources (lead). **Shengru Chen:** Conceptualization (lead); data curation (equal). **Shan Lin:** Investigation (equal); methodology (equal). **Qiao Jin:** Conceptualization (equal); methodology (equal). **Haitao Hong:** Conceptualization (equal); investigation (equal); methodology (equal). **Dongke Rong:** Conceptualization (equal); methodology (equal); resources (equal); software (equal). **Haizhong Guo:** Formal analysis (equal); funding acquisition (equal); investigation (equal); visualization (equal). **Can Wang:** Investigation (equal); software (equal); validation (equal). **Ziyu Wang:** Writing – review & editing (equal). **Kui-Juan Jin:** Funding acquisition (equal). **Zhenping Wu:** Funding acquisition (equal); writing – original draft (equal). **Er-Jia Guo:** Supervision (equal); writing – original draft (equal); writing – review & editing (equal).

DATA AVAILABILITY

The data that support the findings of this study are available from the corresponding authors upon reasonable request.

REFERENCES

[1] B. D. Gates, Science **323**, 1566–1567 (2009).

[2] A. Nathan, A. Ahnood, M. T. Cole, S. Lee, Y. Suzuki, P. Hiralal, F. Bonaccorso, T. Hasan, L. Garcia-Gancedo, A. Dyadyusha, S. Haque, P. Andrew, S. Hofmann, J. Moultrie, D. P. Chu, A. J. Flewitt, A. C. Ferrari, M. J. Kelly, J. Robertson, G. A. J. Amaratunga, and W. I. Milne, Proc. IEEE **100**, 1486–1517 (2012).

[3] H. B. Li, Y. J. Ma, and Y. G. Huang, Mater. Horiz. **8**, 383–400 (2021).

[4] W. Gao, H. Ota, D. Kiriya, K. Takei, and A. Javey, Acc. Chem. Res. **52**, 523–533 (2019).

[5] K. X. Teng, Q. An, Y. Chen, Y. H. Zhang, and Y. T. Zhao, Acc. Chem. Res. **7**, 1302–1337 (2021).

[6] X. D. Chen, J. A. Rogers, S. P. Lacour, W. P. Hu, and D. H. Kim, Chem. Soc. Rev. **48**, 1431–1433 (2019).

[7] S. Choi, H. Lee, R. Ghaffari, T. Hyeon, and D. H. Kim, Adv. Mater. **28**, 4203–4218 (2016).

[8] J. He and T. M. Tritt, Science **357**, eaak9997 (2017).

[9] S. Park, G. Wang, B. Cho, Y. Kim, S. Song, Y. Ji, M. H. Yoon, and T. Lee, Nat. Nanotechnol. **7**, 438–442 (2012).

[10] E. B. Secor, P. L. Prabhumirashi, K. Puntambekar, M. L. Geier, and M. C. Hersam, J. Phys. Chem. Lett. **4**, 1347–1351 (2013).

[11] Y. Cui, Z. H. Qin, H. Wu, M. Li, and Y. J. Hu, Nat. Commun. **12**, 1284 (2021).

[12] S. Macher, M. Schott, M. Dontigny, A. Guerfi, K. Zaghib, U. Posset, and P. Lobmann, Adv. Mater. Technol. **6**, 2000836 (2021).

[13] T. G. Sano, T. Yamaguchi, and H. Wada, Phys. Rev. Lett. **118**, 178001 (2017).

[14] H. Kum, D. Lee, W. Kong, H. Kim, Y. Park, Y. Kim, Y. Baek, S. H. Bae, K. Lee, and J. Kim, Nat. Electron. **2**, 439–450 (2019).

[15] S. H. Bae, H. Kum, W. Kong, Y. Kim, C. Choi, B. Lee, P. Lin, Y. Park, and J. Kim, Nat. Mater. **18**, 550–560 (2019).

[16] D. C. Geng and H. Y. Yang, Adv. Mater. **30**, 1800865 (2018).

[17] V. Q. Le, T. H. Do, J. R. D. Retamal, P. W. Shao, Y. H. Lai, W. W. Wu, J. H. He, Y. L. Chueh, and Y. H. Chu, Nano Energy **56**, 322–329 (2019).

[18] B. R. Tak, V. Gupta, A. K. Kapoor, Y. H. Chu, and R. Singh, ACS Appl. Electron. Mater. **1**, 2463–2470 (2019).

[19] M. Yen, Y. H. Lai, C. Y. Kuo, C. T. Chen, C. F. Chang, and Y. H. Chu, Adv. Funct. Mater. **30**, 2004597 (2020).

[20] T. D. Ha, J. W. Chen, M. Yen, Y. H. Lai, B. Y. Wang, Y. Y. Chin, W. B. Wu, H. J. Lin, J. Y. Juang, and Y. H. Chu, ACS Appl. Mater. Interfaces **12**, 46874–46882 (2020).

[21] Y. F. He, L. X. Wang, Z. X. Xiao, Y. W. Lv, L. Liao, and C. Z. Jiang, Chin. Phys. Lett. **37**, 088502 (2020).

[22] H. Xu, Z. L. Luo, C. G. Zeng, and C. Gao, Chin. Phys. Lett. **36**, 078101 (2019).

[23] R. Q. Cheng, Y. Wen, L. Yin, F. M. Wang, F. Wang, K. L. Liu, T. A. Shifa, J. Li, C. Jiang, Z. X. Wang, and J. He, Adv. Mater. **29**, 1703122 (2017).

[24] T. Amrillah, Y. Bitla, K. Shin, T. N. Yang, Y. H. Hsieh, Y. Y. Chiou, H. J. Liu, T. H. Do, D. Su, Y. C. Chen, S. U. Jen, L. Q. Chen, K. H. Kim, J. Y. Juang, and Y. H. Chu, ACS Nano **11**, 6122–6130 (2017).

[25] Y. T. Zhang, Y. Q. Cao, H. Hu, X. Wang, P. Z. Li, Y. Yang, J. Zheng, C. Zhang, Z. Q. Song, A. D. Li, and Z. Wen, ACS Appl. Mater. Interfaces **11**, 8284–8290 (2019).

[26] C. Cheng, S. R. Chen, J. Deng, G. Li, Q. H. Zhang, G. Lin, T. P. Ying, E. J. Guo, J. G. Guo, and X. L. Chen, Chin. Phys. Lett. **39**, 047301 (2022).

[27] M. K. Lee, T. K. Nath, C. B. Eom, M. C. Smoak, and F. Tsui, Appl. Phys. Lett. **77**, 3547–3549 (2000).

[28] H. Baaziz, N. K. Maaloul, A. Tozri, H. Rahmouni, S. Mizouri, K. Khirouni, and E. Dhahri, Chem. Phys. Lett. **640**, 77–81 (2015).

[29] P. Graziosi, A. Gambardella, M. Prezioso, A. Riminucci, I. Bergenti, N. Homonnay, G. Schmidt, D. Pullini, and D. Busquets-Mataix, Phys. Rev. B **89**, 214411 (2014).

[30] M. Fath, S. Freisem, A. A. Menovsky, Y. Tomioka, J. Aarts, and J. A. Mydosh, Science **285**, 1540–1542 (1999).

[31] X. Hong, A. Posadas, A. Lin, and C. H. Ahn, Phys. Rev. B **68**, 134415 (2003).

[32] I. Stolichnov, S. W. E. Riester, E. Mikheev, N. Setter, A. W. Rushforth, K. W. Edmonds, R. P. Campion, C. T. Foxon, B. L. Gallagher, T. Jungwirth, and H. J. Trodahl, Phys. Rev. B **83**, 115203 (2011).

[33] C. Zhang, S. S. Ding, K. M. Qiao, J. Li, Z. Li, Z. Yin, J. R. Sun, J. Wang, T. Y. Zhao, F. X. Hu, and B. G. Shen, ACS Appl. Mater. Interfaces **13**, 28442–28450 (2021).

[34] X. Wang, A. Y. Cui, F. F. Chen, L. P. Xu, Z. G. Hu, K. Jiang, L. Y. Shang, and J. H. Chu, Small **15**, 1903106 (2019).

[35] S. S. Hong, M. Q. Gu, M. Verma, V. Harbola, B. Y. Wang, D. Lu, A. Vailionis, Y. Hikita, R. Pentcheva, J. M. Rondinelli, and H. Y. Hwang, Science **368**, 71–76 (2020).

[36] C. Boskovic, M. Pink, J. C. Huffman, D. N. Hendrickson, and G. Christou, J. Am. Chem. Soc. **123**, 9914–9915 (2001).

[37] H. Sawada, Y. Morikawa, N. Hamada, and K. Terakura, J. Am. Chem. Soc. **177–181**, 879–880 (1998).

[38] M. M. Yang, D. J. Kim, and M. Alexe, Science **360**, 904–907 (2018).

[39] R. Guo, L. You, W. N. Lin, A. Abdelsamie, X. Y. Shu, G. W. Zhou, S. H. Chen, L. Liu, X. B. Yan, J. L. Wang, and J. S. Chen, Nat. Commun. **11**, 2571 (2020).

[40] F. Zhang, P. Lv, Y. T. Zhang, S. J. Huang, C. M. Wong, H. M. Yau, X. X. Chen, Z. Wen, X. N. Jiang, C. G. Zeng, J. W. Hong, and J. Y. Dai, Phys. Rev. Lett. **122**, 257601 (2019).

[41] Y. Z. Gao, J. C. Zhang, G. X. Cao, X. F. Mi, and H. U. Habermeier, Solid State Commun. **154**, 46–50 (2013).

[42] Z. L. Liao, F. M. Li, P. Gao, L. Li, J. D. Guo, X. Q. Pan, R. Jin, E. W. Plummer, and J. D. Zhang, Phys. Rev. B **92**, 125123 (2015).